Geochemistry, Geophysics, Geosystems®

AGU ADVANCING EARTH AND SPACE SCIENCE

RESEARCH ARTICLE
10.1029/2022GC010585

A Highly Depleted and Subduction-Modified Mantle Beneath the Slow-Spreading Mohns Ridge

A. Bjerga[1], H. H. Stubseid[1], L. E. R. Pedersen[1], A. Beinlich[1], and R. B. Pedersen[1]

[1]Department of Earth Science and K.G. Jebsen Center for Deep Sea Research, University of Bergen, Bergen, Norway

Key Points:

- We report mantle peridotites and basalts from a 4–5 Myr tectonic window in the Mohns Ridge (Arctic Mid-Ocean Ridges)
- The peridotite and basalt compositions reveal a highly depleted mantle with a subduction signature
- The anomalous depleted mantle is likely a consequence of an earlier hydrous melting event

Supporting Information:

Supporting Information may be found in the online version of this article.

Correspondence to:

A. Bjerga,
anders.bjerga@gmail.com

Citation:

Bjerga, A., Stubseid, H. H., Pedersen, L. E. R., Beinlich, A., & Pedersen, R. B. (2022). A highly depleted and subduction-modified mantle beneath the slow-spreading Mohns Ridge. *Geochemistry, Geophysics, Geosystems*, *23*, e2022GC010585. https://doi.org/10.1029/2022GC010585

Received 23 JUN 2022
Accepted 20 SEP 2022

Abstract The Mohns Ridge is a very slow-spreading ridge that, together with the Knipovich Ridge, marks the boundary between the North American and Eurasian plates in the Norwegian-Greenland Sea. In this study, we report the major and trace element composition of spatially associated basalts and peridotites from a gabbro-peridotite complex ~20 km west of the Mohns Ridge rift flank. Formation of the ~4–5 Myr crustal section involved accretion of normal mid-ocean ridge basalts with Na-content suggesting derivation from a depleted mantle source. This is consistent with the degree of partial melting estimated for clinopyroxene poor harzburgites using the Cr-number of spinel (14%–18%) and rare earth element modeling of orthopyroxene (16%–24%) and reconstructed whole-rock composition (14%–20%). If all the melting took place beneath the paleo-Mohns Ridge, a crustal thickness of ~7–8 km is expected, which is nearly double the observed thickness. Orthopyroxene trace elements are not consistent with typical fractional melting expected for mid-ocean ridges but rather resemble that seen in supra-subduction zone peridotites. The geochemistry of both the basalts and the peridotites suggests that a water-rich slab flux in the past has influenced the mantle source. In turn, this caused hydrous melting which increased the depletion of the pyroxene components, leading to a highly depleted mantle that is now underlying much of the Arctic Mid-Ocean Ridges and represents the source for the spreading related magmatism.

1. Introduction

Abyssal peridotites are pieces of the upper mantle collected from the mid-ocean ridges and yield insights into mantle processes and geochemistry. Studies of erupted basalts and exposed peridotites from the mid-ocean ridge and fracture zones have shown that the oceanic mantle is highly heterogenous in chemical composition on the kilometer scale down to the sample scale (Andres et al., 2004; Brandon et al., 2000; Byerly & Lassiter, 2014; Cipriani et al., 2004; D'Errico et al., 2016; Dick et al., 1984; Dosso et al., 1999; Graham et al., 2006; Guo et al., 2021; Harvey et al., 2006; Hauri, 2002; Johnson et al., 1990; Liu et al., 2008; Mallick et al., 2014; Rampone & Hofmann, 2012; Sanfilippo et al., 2021; Stracke, 2012; Stracke & Bourdon, 2009; Stracke et al., 2019; Urann et al., 2020; Warren et al., 2009). The compositional evolution of the mantle reflects the time-integrated removal of both major and trace elements to form the ocean crust and the return flux into the mantle, and the observed chemical and mineralogical heterogeneities have developed through a combination of repeated melt extraction and recycling of crustal components (Stracke, 2012). However, the scarce available data on the trace element and isotopic composition of spatially associated abyssal peridotites and basalts limit our understanding of the underlying processes and evolution of the oceanic mantle.

While numerous basaltic rocks (>30,000 samples from 771 spreading segments (Gale et al., 2013)) have been recovered from the ocean floor, exposure of mantle rocks is uncommon and has been reported from around 50 localities throughout the global mid-ocean ridge system, with the large majority (~70%) coming from the Mid-Atlantic Ridge and Southwestern Indian Ridge (Warren, 2016) and only a handful of studies report peridotite-basalt pairs (Brunelli et al., 2018; Cipriani et al., 2004). From a regional perspective, less than 8% of all studied mid-ocean ridge peridotites come from the Arctic Mid-Ocean Ridges (AMOR) and no peridotites have been reported from the Mohns and Knipovich Ridges. On a broader scale, the 550 km long Mohns Ridge is of special interest because of its very slow spreading rate and reported ultra-refractory, subduction-influenced mantle composition (Blichert-Toft et al., 2005; Sanfilippo et al., 2021; Yang et al., 2021). Specifically, it has some of the most radiogenic Hf isotopes seen in mid-ocean ridge basalts indicating a mantle-source that is ultra-depleted (Sanfilippo et al., 2021). Along the Mohns and Knipovich Ridges, reported basalt compositions come from young (<300 Kyr) samples from within the rift valley, meaning that the evolution of the mantle source through time is poorly known.

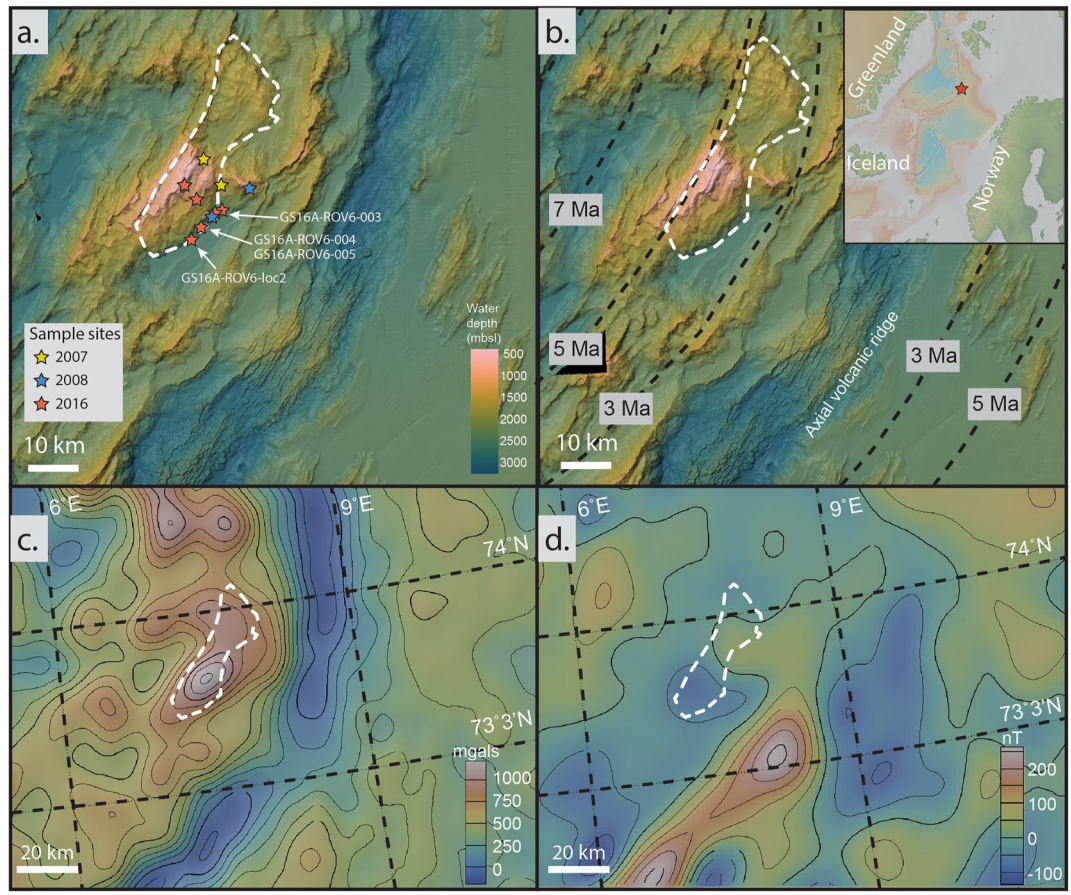

Figure 1. Geographic overview of the study area. (a) Bathymetric map at 50-m resolution with an overview of sample sites from the Schulz Massif which is outlined. More precise sample locations are shown in Figure 2 and provided in Table S1. (b) Seafloor crustal age model by Müller et al. (2008). Scale is the same as in a. (c) Free-air gravity anomaly grid from the Arctic Gravity Project (Kenyon et al., 2008). (d) Magnetic anomaly grid from Maus et al. (2009). Figures c and d were created using GeoMapApp (www.geomapapp.org).

The Schulz Massif (73.4°N) exposes 4–5 Myr (Bjerga, Stubseid, Pedersen, & Pedersen, 2022) mafic and ultramafic oceanic lithosphere approximately 20 km west of the Mohns Ridge rift flank (Figure 1). To determine the nature and composition of the paleo-sub-oceanic mantle beneath the slow-spreading Mohns Ridge, we studied spatially associated abyssal peridotites and basalts. The age and setting of the samples allow us to test and evaluate the mantle composition and provide direct access to understanding the evolution of mantle depletion and modification. To quantify the extent of melting, we use (a) peridotite compositions, (b) mineral chemistry of pyroxene and Cr-spinel with low TiO_2-content and (c) Na-concentrations of basalts. To further constrain the Arctic mantle source composition, we use Sr and Nd isotopes of basalts, Nd isotopes of orthopyroxene from peridotites, and trace element characteristics of orthopyroxene. The geochemistry of peridotite and basalt suggests that a water-rich subduction flux has influenced the mantle in the past. Because of this, the mantle has experienced hydrous melting, likely in an arc-type setting, leading to anomalously depleted peridotite compositions. Our results add to a growing body of literature trying to better constrain and understand the mantle segmentation and evolution in the Arctic region (Goldstein et al., 2008; Neumann & Schilling, 1984; Richter et al., 2020; Sanfilippo et al., 2021; Yang et al., 2021).

2. Geological Setting

The Arctic Mid-Ocean Ridge system is a slow to ultraslow (spreading rate between ~20 and 6 mm/year) divergent plate boundary and the northernmost extension of the mid-ocean ridge, extending for approximately 4,000 km from Iceland in the south, to the Gakkel Ridge in the north. The ridge system starts at the boundary between

the elevated Icelandic Rise and Kolbeinsey Ridge from where it follows through the Mohns and Knipovich Ridges and becomes gradually deeper toward the Lena Trough and the Gakkel Ridge. Blichert-Toft et al. (2005) studied the Sr, Nd, and Hf isotope composition of basalts between 50°N and 78°N and divided the mantle into three isotopically distinct segments with an ultra-depleted mantle residing beneath the Mohns Ridge. The very slow-spreading (14–16 mm full spreading per year) Mohns and Knipovich ridges are situated between two distinct mantle domains that are restricted by the Lena Trough in the North and the Jan Mayen Island to the south. Hf isotope composition of ridge basalts suggest this sub-oceanic mantle has a significant contribution of ancient and ultra-refractory mantle components (Sanfilippo et al., 2021).

3. Sampling of the Schulz Massif

The Schulz Massif is located at 73.4°N, 20 km to the west from the axial rift flank at the transition between the Mohns and Knipovich Ridges (Figure 1). It is a prominent ∼10-km-wide and ∼35-km-long NE-SW trending bathymetric high, which rises from 2,500 to 600 m in depth (Figure 1a). It has a smaller surface area (∼60%) compared with well-described oceanic core complexes exposing peridotites such as the Kane Megamullion (40 × 23 km, Mid-Atlantic Ridge (MAR) (Dick et al., 2008)) and primitive gabbroic massifs such as the Atlantis Bank (40 × 20 km; Southwest Indian Ridge (SWIR; Coogan et al., 2004; Godard et al., 2009; John et al., 2004)). It is larger than Atlantis Massif (∼10 × 15 km, MAR (Blackman et al., 2002; Godard et al., 2009)) where the oceanic lithosphere is dominated by intermediate gabbroic lithologies. A positive "bulls-eye" gravity pattern characterizes parts of the massif in the free-air anomaly data, while the active spreading axis is associated with gravity lows (Figure 1c). The amplitude of the gravity anomaly is ∼60 mGal between the massif and the nearby bathymetric highs and ∼120 mGal between the massif and the spreading axis. A similar pattern is seen in other locations of the Mid-Atlantic Ridge (Detrick et al., 1995) and indicates either thinner than average crust or an abundance of mantle rocks. The negative magnetic anomalies seen over the Schulz Massif are interpreted to represent the exposure of mantle-derived lithologies (Figure 1d).

Investigations of the massif and surrounding with the vessel G.O. Sars were done in 2008, 2009, and 2016 and include a series of remotely operated vehicle (ROV) dives (using the ROV Ægir 6000) and dredges along the eastern-facing surface (average slope ∼13°). A dredge haul (GS08-DR1) crossed several eastward dipping fault scarps and recovered fragments of serpentinized peridotite, gabbro, and mafic dikes. The gabbros have been intruded by mafic dikes and show cataclastic to mylonitic structures. All recovered peridotites except for one dredged sample, which appears heavily deformed, are undeformed and display mesh textures after olivine.

During dive GS16-ROV6, we visited three locations along the foot of the massif where the fault plane dips into a deep sedimentary basin approximately 800 m thick (Bruvoll et al., 2009). Much of the surface in the area is covered with pelagic sediment or rubble from mass wasting with locally isolated exposures of bedrock. At all three locations, we recovered both mantle peridotite and gabbro from within a few meters of each other (Figure 2). Both peridotites and gabbros are cut by mafic dikes and appear largely undeformed, except for some gabbro exhibiting cataclastic textures. Some samples are from loose rocks while others come from exposed bedrock, but the thin layer of manganese crust makes it difficult to see any structures.

The transect GS16-ROV4 passes over a gently sloping, sedimented surface which separates two ridge parallel structures interpreted as normal faults, into a more steeply dipping talus ramp toward the top of the massif (Figure 2). A poorly sorted, matrix-supported breccia with vesicular basaltic clasts up to 10 cm in size were sampled here. In-place lavas are exposed near the summit of the breakaway where the average slope is about 35°. Aphyric basaltic sample GS16-ROV4-003 and vesicular basalt sample GS16-ROV4-004 were taken from a steeply dipping wall. A prominent topographic high directly east of the massif, where a sheeted dike complex was observed at a depth of approximately 1,650 m during ROV dive GS08-ROV6, is interpreted as a hanging wall that sits on top of the footwall. Collectively, the distribution of samples recovered suggests that the studied sections are composed of gabbroic material intruded into mantle peridotites which have subsequently been exposed through low-angle faulting.

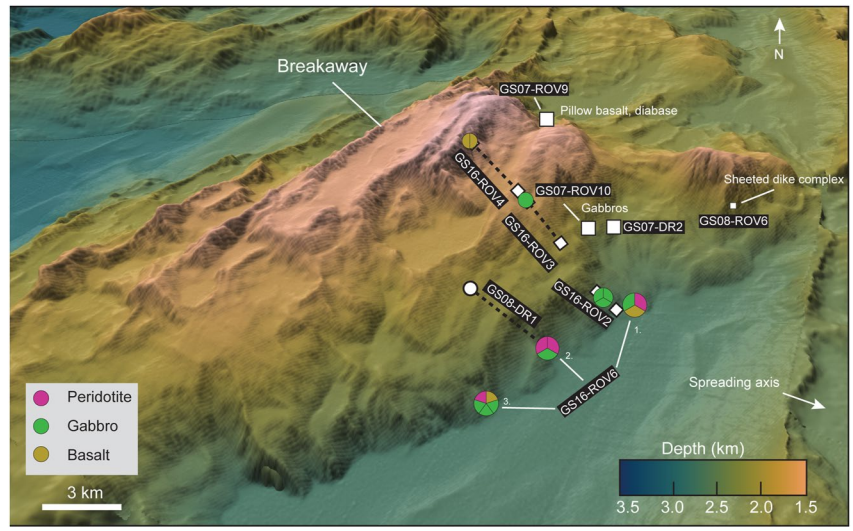

Figure 2. High-resolution bathymetry and sample overview. White squares show the location of remotely operated vehicle (ROV) dives while the dashed black lines connected by white squares show the dive tracks. Dashed black lines connected by circles show the dredge track which was carried out up-slope. Pie diagrams show the number of lithologies (number of samples) that were collected in the GS16 ROV survey. GS07, GS08, and GS16 refer to the year of the survey: 2007, 2008, and 2016, respectively, and DR and ROV refer to survey type (dredge or ROV, respectively). The vertical exaggeration of the bathymetry is 2:1.

4. Results

4.1. Whole-Rock Major and Trace Elements

4.1.1. Peridotites

Peridotites have Mg# (MgO/(MgO + FeO_{tot}))between 0.88 and 0.90 and are close to the terrestrial array in the MgO/SiO_2 versus Al_2O_3 space. On the basis of differences in major and trace element compositions, we have subdivided the peridotite samples into type I and type II peridotites. Type I peridotites have Al_2O_3 between 1.57 and 1.64, Yb ~0.10 ppm, and $\sum$ rare earth elements (REE) ~2 ppm (Figure 3). Type II peridotite has a higher Al_2O_3 (2.61 wt.%), Yb higher than depleted MORB mantle (i.e., Yb = 0.41 ppm), and a higher content of REE (i.e., $\sum$REE ~8 ppm) compared with type I peridotite (Figure 3). To overcome the potential effects of alteration on the whole-rock compositions we recalculated the whole-rock composition using sample GS16A-ROV6-loc2 as a starting point (estimated modal composition of 80% olivine and 20% orthopyroxene). Because of the low estimated modal proportion <1% and low concentration of REE, we exclude spinel from the calculation. We used olivine trace element values from Garrido et al. (2000) and a range of low and high-concentration orthopyroxene as measured in the sample (Table S3). The reconstructed Type I peridotites display primitive mantle (PM)-normalized trace-element patterns similar to fore-arc peridotites (Figure 4) while the un-corrected whole-rock Type I peridotite is similar to peridotites from MAR and SWIR (Figure 4).

4.1.2. Basaltic Lavas and Mafic Dikes

The basalt samples are tholeiitic in composition with SiO_2 ranging between 49 and 51 wt.%, $Na_2O + K_2O$ between 2.0 and 3.1 wt.% and Mg# 53–61. The trace element compositions are like N-MORB, with REE patterns slightly depleted in light REE (LREE) compared with middle REE (MREE) (Figure 4b). Rb, Ba, Nb, U, Ce, and Pb are similarly incompatible during melting processes and yield insights into the source material of mantle-derived basaltic rocks. In our sample suite, all the basalts fit the proposed "back-arc basin filter" (i.e., Ba/Nb > 6, Rb/Nb < 0.6, Nb/U < 42, and Ce/Pb < 22) by Yang et al. (2021), clearly demonstrating a subduction influence on the mantle-derived melts that formed 4–5 Myr ago (Figure 5). Sr and Nd isotope compositions (Table S1) are similar to those of MORBs north of Iceland and from the western volcanic zone of the Gakkel Ridge (Figure 5). One sample has similar isotopic and trace-element characteristics as three anomalous western volcanic zone samples reported by Goldstein et al. (2008).

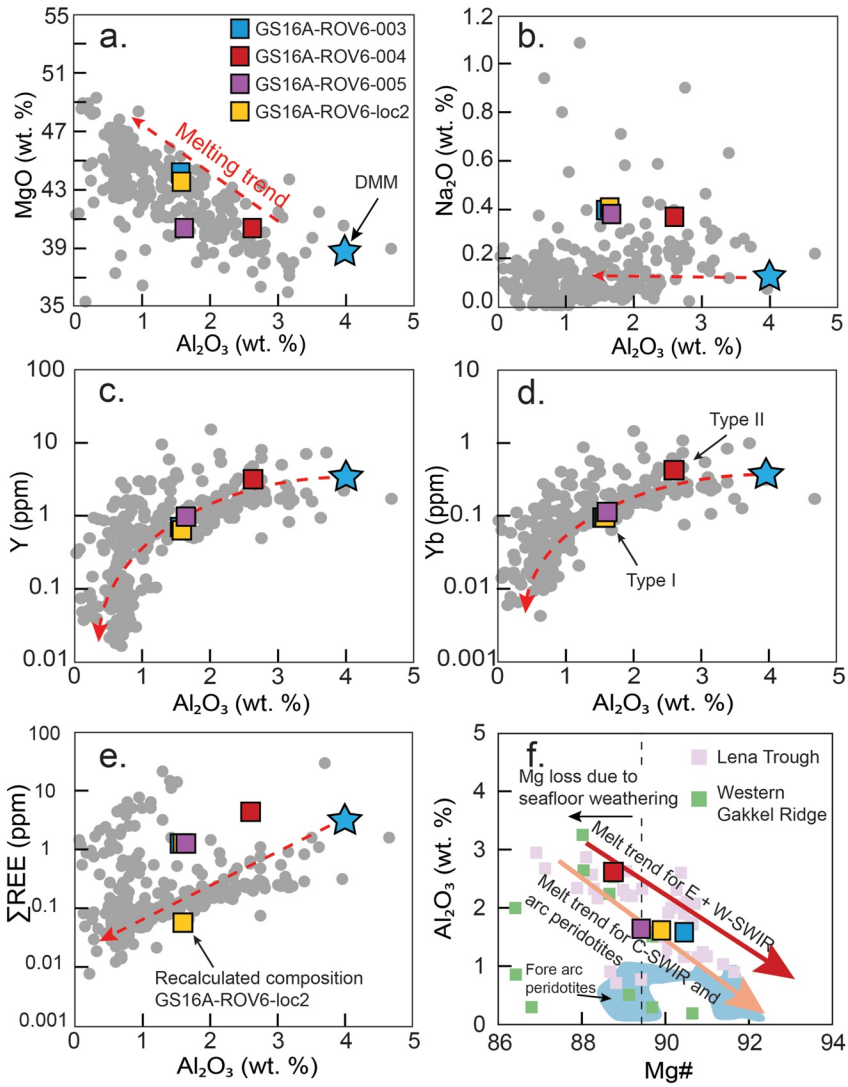

Figure 3. Whole-rock geochemistry of peridotites with melt trends indicated by the red arrows. (a) MgO versus Al_2O_3. (b) The Schulz peridotites plot above the average abyssal peridotite in the Na_2O versus Al_2O_3 plot. (c and d) Y and Yb concentration versus Al_2O_3. (e) The total rare earth element content versus Al_2O_3 shows that the peridotites plot above the expected melting trend. The recalculated composition of GS16A-ROV6-loc2 fits with the general trend observed in abyssal peridotites. Details on the recalculated composition of GS16A-ROV6-loc2 are found in chapter 4.1. (f) Al_2O_3 versus Mg# (Mg/(Mg + Fe_{tot}). Melting trends in f are for dry (red) and wet (orange) melting, respectively derived from Gao et al. (2016). Partial melting of a mantle source will drive the composition in a straight trend away from the source composition meaning that the samples will project backward to their initial source. This suggests that the Schulz peridotites are derived from a highly depleted Al_2O_3-poor source. Fore-arc peridotites are from Parkinson and Pearce (1998) and Pearce et al. (2000). Lena Trough peridotites from Lassiter et al. (2014) and Western Gakkel ridge from Liu et al. (2017). Gray data points in all the plots are abyssal peridotite from the compilation of Deschamps et al. (2013).

4.2. Petrography and Mineral Chemistry

4.2.1. Peridotites

The high loss on ignition (10%–14%) illustrates the extensive addition of volatiles (H_2O and CO_2) through water-rock reactions. These reactions obliterated many of the primary magmatic textures (Figures S1, S3, and S4 in Supporting Information S1), leading to the replacement of the magmatic minerals by mesh-textured serpentine and variable amounts of carbonate (<5 vol%). Despite extensive alteration, large (1–10 mm) orthopyroxene crystals are present in all studied rocks (Figures S1 and S2 in Supporting Information S1). Trails of inclusions are visible in orthopyroxene from all samples (Figure S1 in Supporting Information S1). Subhedral olivine (~0.1 mm

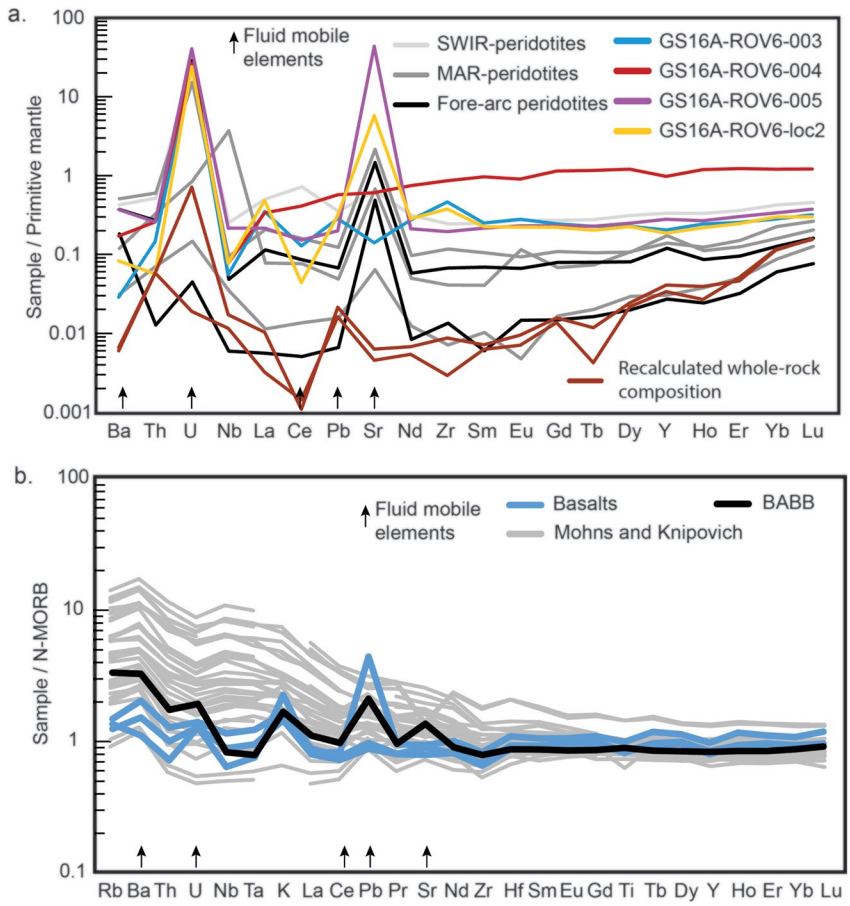

Figure 4. Trace element characteristics of peridotites and basalts. (a) Primitive mantle normalized trace element abundances of the peridotites from the Schulz Massif. Details on the recalculated whole-rock composition for sample GS16A-ROV6-loc2 are found in chapter 4.1. Fore-arc peridotites from Parkinson and Pearce (1998) and Birner et al. (2017), Mid-Atlantic Ridge-peridotites from Godard et al. (2008), Drouin et al. (2009), and Burgath et al. (1997), and Southwest Indian Ridge peridotites from Gao et al. (2016). In sample GS16A-ROV6-loc2, Nb and Th were below detection limits and, in the sample, GS16A-ROV6-004, Nb was below detection limits (Table S1). Elements below detection limits have been plotted as LOD/2. (b) Normal mid-ocean ridge basalt (N-MORB) normalized trace element abundances of the basaltic lavas and mafic dikes from the Schulz Massif. N-MORB and back-arc basin basalt (BABB) from Gale et al. (2013). Mohns and Knipovich basalts are from Kelley et al. (2013), Haase et al. (1996), Kruber et al. (2008), and Bezard et al. (2016).

in size) occurs within orthopyroxene associated with clinopyroxene and spinel (Figure S2 in Supporting Information S1). Clinopyroxene is present as ~1.7–3.7 μm thick regular lamellae in orthopyroxene and as small grains within orthopyroxene where they are sometimes associated with Cr-spinel ± olivine (Figure S2 in Supporting Information S1). Cr-spinel, 1–2 mm in size, is deep brown and ranges from anhedral to subhedral. Cr-spinel has been partly replaced by ferritchromite and magnetite (Figure S3 in Supporting Information S1) leading to a zoned pattern in backscatter electron images (Figure S3 in Supporting Information S1). Ferritchromite is associated with significant porosity (Figures S3 and S4 in Supporting Information S1), which may be related to the ~35 vol% decrease during the formation of ferritchromite after Cr-spinel (Merlini et al., 2009). The most altered Cr-spinel shows up to 100 μm thick alteration rims (Figure S3 in Supporting Information S1).

Pyroxene major, minor, and isotopic compositions vary on the sample and grain scale (Tables S2–S4). Clinopyroxene can be divided into a low- and high-TiO_2 group. Clinopyroxene grains have a relatively consistent composition (Figure 6) except for TiO_2, which ranges from 0.3 wt.% up to 1.1 wt.%. Orthopyroxene has Mg# between 0.87 and 0.91, Al_2O_3 between 1.9 and 3.0 wt.%, Cr_2O_3 between 0.4 and 0.9 wt.% and TiO_2 between 0.0 and 0.3 wt.%. Cr-spinel has Cr# (Cr/(Cr + Al)) between 0.22 and 0.58, covering almost the entire range observed in abyssal peridotites (Figure 7). They define three compositional varieties: (a) high Cr–low Al—intermediate Ti, (b) intermediate Cr—intermediate Al–low Ti, and (c) low Cr–high Al–high Ti (Figure 7).

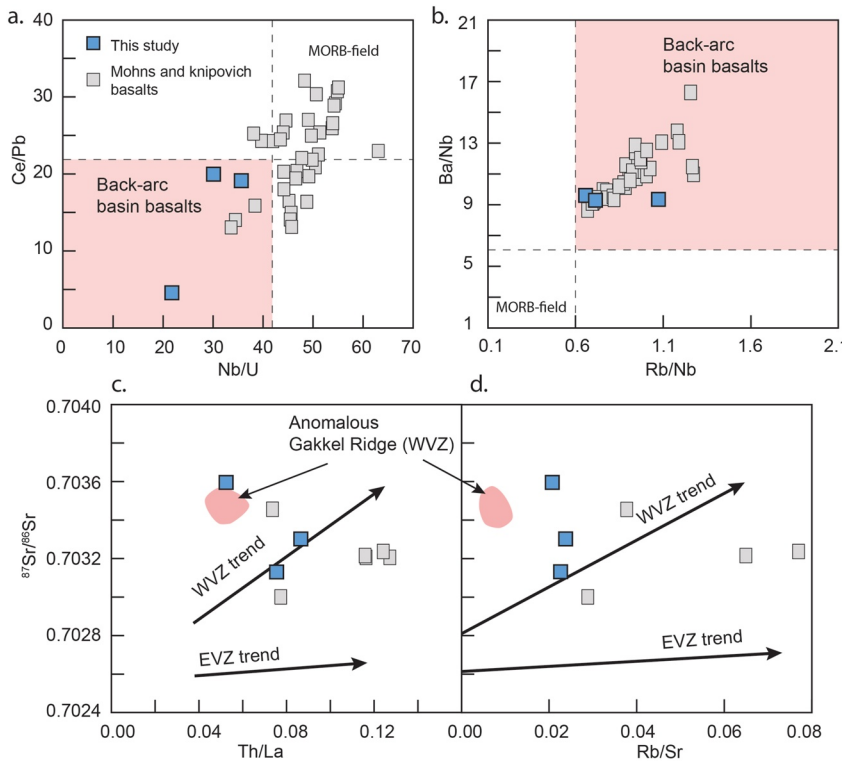

Figure 5. Basalt geochemistry. Fields for back-arc basin and MORB in a and b are from Yang et al. (2021). Basalt compositions in a and b are from Kelley et al. (2013) and Haase et al. (1996). WVZ and EVZ trends in c and d are from Goldstein et al. (2008). Mohns and Knipovich samples in c and d are from Kruber et al. (2008) and Bezard et al. (2016).

Trace element concentrations in orthopyroxene show variable enrichment in Ti and REE (Figure 8, Table S3). Grains from samples GS16A-ROV6-004 and 005 display a range of Ti concentrations between 431 and 5944 ppm while grains from GS16A-ROV6-loc2 have Ti concentrations between 271 and 314 ppm. Also, Y in GS16A-ROV6-004 and 005 range between 1.1 and 14.2 ppm, significantly higher than in grains from GS16A-ROV6-loc2 (between 0.6 and 0.8 ppm). When normalized to chondrite, GS16A-ROV6-loc2 displays a flat, slightly U-shaped LREE pattern (Figure 8).

5. Discussion

5.1. Geochemical and Mineralogical Constraints on Peridotite Partial Melting

Regardless of the influences of post-melt extraction modifications (e.g., metasomatism, hydration, seafloor weathering), the geochemistry of type I peridotite samples is consistent with that of partial melting (Figure 3), suggesting that they have preserved at least parts of their primary magmatic characteristics. While the most incompatible elements, such as the large ion lithophile elements and LREE, are excellent proxies for post-melting metasomatism and alteration, less incompatible elements such as heavy REE (HREE) and Al are considered less affected by metasomatic processes (e.g., Niu, 2004). The Yb-concentrations in type I peridotites (i.e., Yb = 0.19–0.23 × PM) are lower than from abyssal peridotites from SWIR (0.42 ± 0.23 (1SD) × PM (Gao et al., 2016)) and similar to abyssal peridotites from MAR (0.22 ± 0.06 (1SD) × PM (Burgath et al., 1997)). The recalculated whole-rock composition has Yb = 0.11 × PM similar to fore-arc peridotites (0.13 ± 0.14 (1SD) × PM (Birner et al., 2017)) while pyroxene Al_2O_3-concentrations are at the lower end of the range typically observed in abyssal peridotites (Figure 3d). This indicates moderate to high degrees of melt extraction, as suggested by melting experiments, numerical models, and petrological observations (Niu, 2004; Warren, 2016).

The REEs are decreasingly incompatible with increasing atomic numbers and are therefore suited to distinguish between partial melting processes and post-melting modifications (e.g., Niu, 2004). In chondrite normalized REE diagrams, the Schulz peridotites are characterized by flat to slightly LREE-enriched patterns with distinct

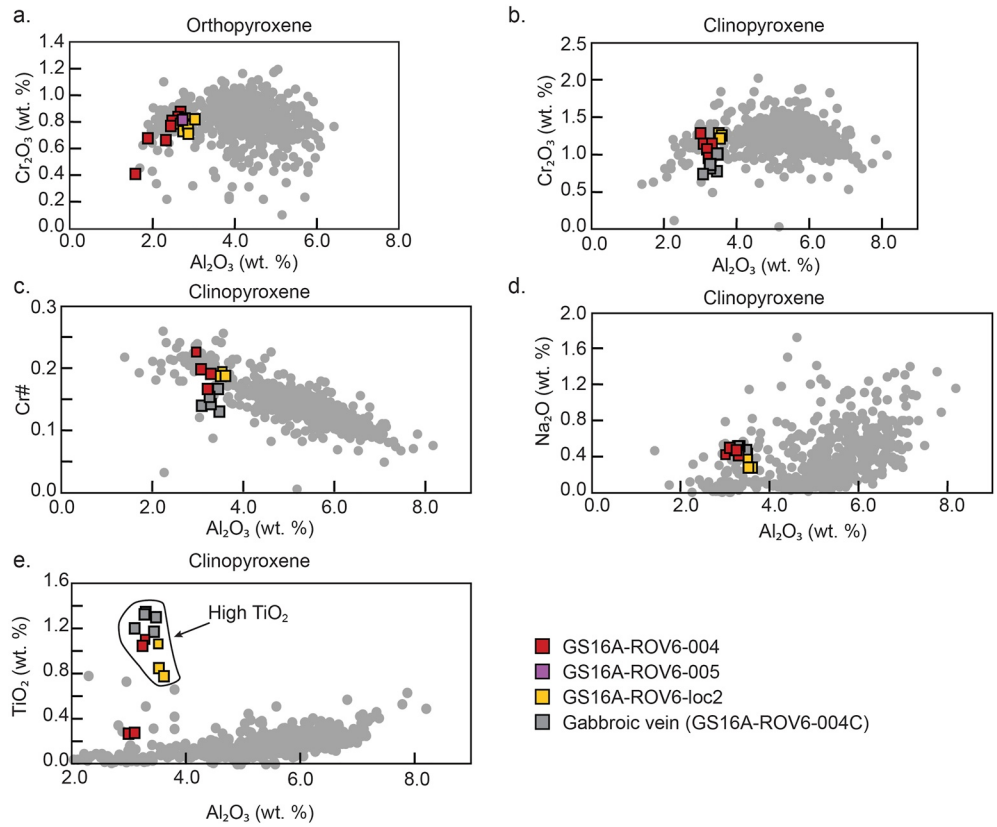

Figure 6. Mineral chemistry of orthopyroxene and clinopyroxene in peridotite and gabbroic vein. Gray data points are from the global compilation by Warren (2016).

negative Ce-anomalies and flat to slightly positive Eu-anomalies (Figure 9). We modeled the REE composition of the bulk peridotite based on the fractional melting model (REEMODEL) provided by Warren (2016) using the depleted MORB mantle (DMM) composition of Workman and Hart (2005) and the PM composition of McDonough and Sun (1995) as starting compositions. The model outcomes are presented in Figure 9 and show that (a) the LREE and MREE distribution of the type I peridotite cannot be explained purely by fractional melting of either DMM or PM, (b) if the HREE content of the peridotites reflects partial melting, type I peridotites have experienced similar degrees of melting and (c) depending on whether the precursor rock composition was similar to DMM or PM, the composition of type I peridotite is consistent with partial melting by ~10–12% and ~15%-17%, respectively.

Orthopyroxene trace elements may be decoupled from the whole-rock abundances (Scott et al., 2016) and may therefore be suited to evaluate the degree of partial melting and melt-rock interactions. Orthopyroxene residual after partial melting is expected to be low in Ti, Zr, and Y. This is also indicated from our data, where the REE-normalized patterns of orthopyroxene that have much higher Ti, Y, and Zr-content than expected at the low Al_2O_3 cannot be modeled by any degree of fractional melting of a depleted mantle (Table S3). This suggests that these rocks were metasomatized by a Ti-rich medium beneath the ridge axis. In contrast, orthopyroxene in sample GS16A-ROV6-loc2 has lower Ti, Zr, and Y concentrations (Figure 8: Table S3), suggesting that orthopyroxene from this sample is more likely to record melting events. By applying the same fractional melting model as above, the HREE content of recalculated bulk-rock composition of sample GS16A-ROV6-loc2 suggests a degree of partial melting between 14% and 20% (Figure 9). This is similar to the values between 16% and 26% we get by comparing the orthopyroxene data to the melting models by Scott et al. (2016). It is important to note that the degree of partial melting estimated from these REE models depends on the precursor rock composition, the applied partition coefficients, and the melting model used (Warren, 2016).

A second indication of the partial melting experienced by the peridotites is based on the composition of Cr-spinel. Cr-spinel in type I and type II peridotite displays correlating variations in Cr_2O_3 and Al_2O_3 that can result from

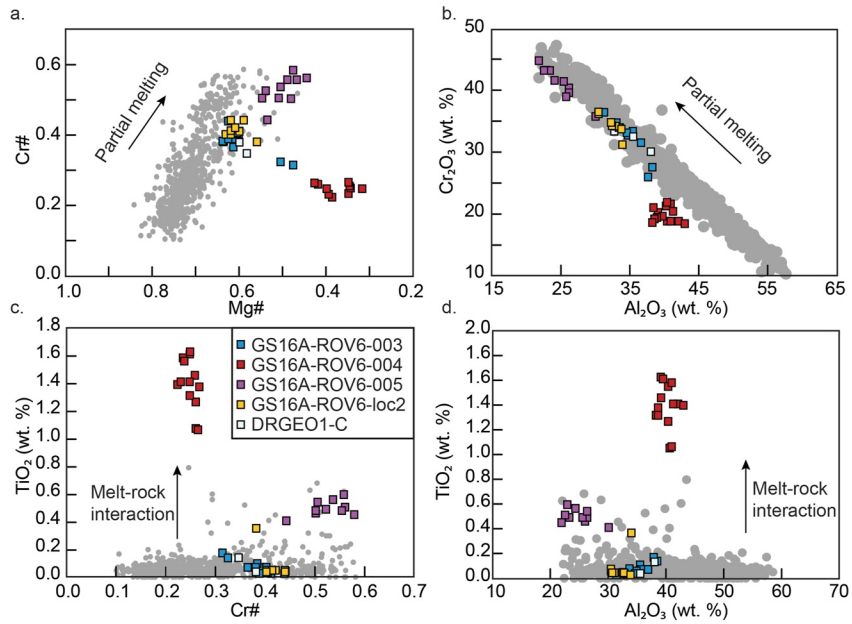

Figure 7. Cr-spinel chemical composition. (a) Increasing Cr# caused by increasing degrees of partial melting. (b) The Cr_2O_3 versus Al_2O_3 plot of Cr-spinel shows that spinel from sample GS16A-ROV6-004 is offset from the abyssal array indicating that processes other than partial melting have affected these grains. (c) Enrichment of TiO_2 associated with melt-rock interaction. (d) Metasomatism appears to affect the TiO_2-content of spinel. Cr-spinel data from abyssal peridotites are from Warren (2016).

magmatic differentiation, melt-rock interaction, or hydrothermal alteration. Intra-sample variations in Cr# range from 0.04 to 0.14 and yield a difference of 0.8% and 3% in partial melting calculated according to the relationship F (degree of partial melting) = 10 * ln (Cr#) + 24, as suggested by Hellebrand et al. (2001). Three processes can increase the Cr/Al of spinel, the first is equilibration during increased degrees of partial melting, the second is the hydrothermal alteration to form ferritchromite, chlorite, and amphibole (Barnes & Roeder, 2001), and the diffusional reaction with magmatic veinlets (Hellebrand et al., 2002). To avoid the influence of gabbroic veins, we have not analyzed Cr-spinel close to visible veinlets. Besides, we have found no reactions involving chlorite or amphiboles in the sample suite, suggesting that enriched Cr/Al of Cr-spinel primarily results from increased degrees of partial melting. The average composition of Schulz Massif spinel in type I peridotite (Cr# sample average between 38 and 53) is more refractory than peridotites from the Lena Trough (Cr# average of ~25, range between 14 and 42) and the Gakkel Ridge (Cr# average of ~23, range between 12 and 56). If we assume a similar mantle source composition, this will correspond to between 5% and 8% more partial melting. It is also more depleted than spinel from clinopyroxene-poor peridotites from other comparable ridge sections exposing gabbroic lithologies such as Atlantis Bank (Cr# average ~22 (Coogan et al., 2004)) and Kane Megamullion (Cr# average ~34 (Dick et al., 2010)). The high degree of depletion is consistent with the very low aluminum content of pyroxenes (Figure 6) demonstrating that the exposed mantle sampled at the Schulz Massif is extremely refractory.

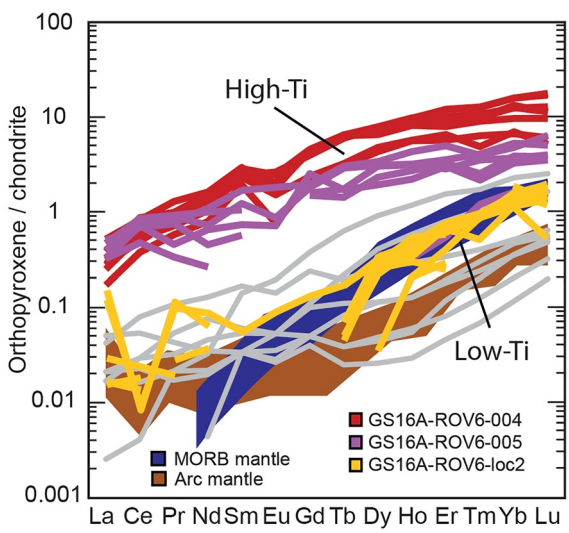

Figure 8. Abyssal peridotite orthopyroxene trace elements normalized to chondrite. Orthopyroxene from MORB-mantel and arc mantle are from Aldanmaz (2012). Gray lines are Gakkel Ridge orthopyroxene from D'Errico et al. (2016).

Additional information on the melting process is provided by the spatially associated basalts. The Na_2O-content of basalts is sensitive to the degree of mantle melting (Klein & Langmuir, 1987) and Regelous et al. (2016) showed that segment-averaged Cr# of spinel is negatively correlated with the Na_2O content of basalts, that is, ridge segments erupting basalts with low Na_2O typically expose peridotites with high Cr# in spinel. Both features, low

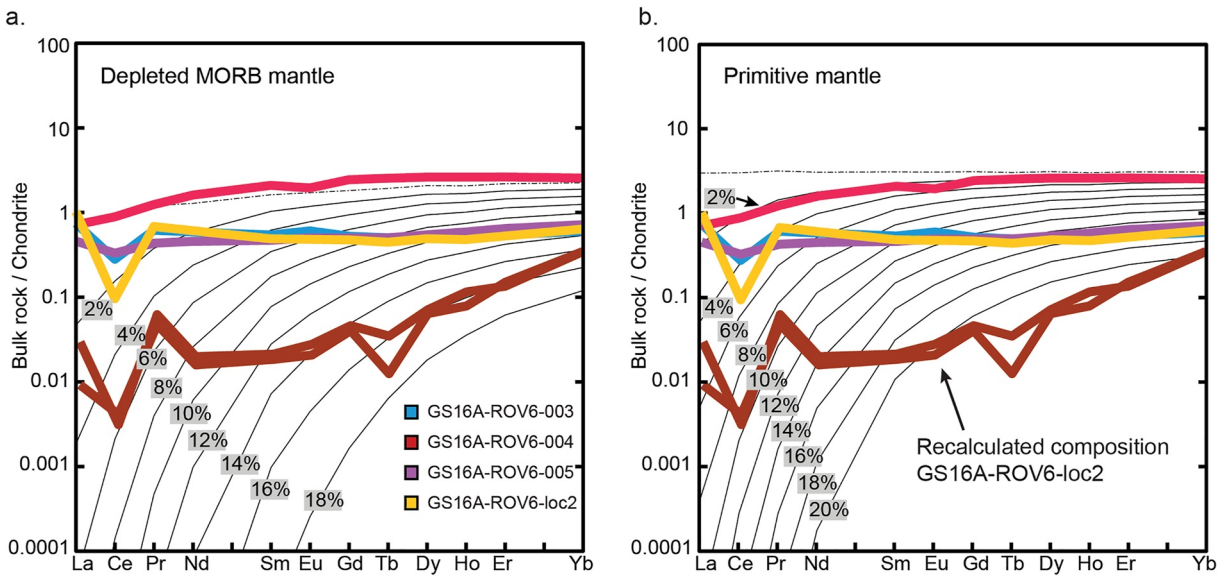

Figure 9. Fractional melting model of rare earth elements in the whole rock. Recalculated composition based on sample GS16A-ROV6-loc2 with an estimated modal proportion of 80% olivine and 20% Opx. Opx compositions from Table S3 and olivine composition from Garrido et al. (2000). More details on the recalculation are found in chapter 4.1.

Na_2O basalts and high Cr# in Cr-spinel are observed at the Schulz Massif, demonstrating that the local upper mantle has experienced high degrees of partial melting.

5.2. Amount of Accreted Ocean Crust and Hydrous Mantle Source

The range of partial melting suggested by spinel Cr# (14%–18%), reconstructed peridotite HREE modeling (14%–20%), and orthopyroxene HREE (16%–24%) are in the upper range of that reported from exposed abyssal peridotites (11.3%–18.3%: Ciazela et al., 2015). Even at the intermediate spreading Central Indian Ridge (25°S) degrees of partial melting were found to be between 13% and 15%. The highest estimated degrees of partial melting (15%–18%) come from the Atlantis Massif oceanic core complex, which has a spreading rate of 24 mm/year and a crustal thickness of ∼7 km (Blackman & Collins, 2010) and the Fifteen-Twenty Fracture Zone, Mid-Atlantic Ridge (Godard et al., 2008). At the Mohns Ridge, the observed crustal thickness of 4 ± 0.5 km (Klingelhöfer et al., 2000) is thinner than the global average of ∼6–7 km. Consequently, our basalt-peridotite analysis suggests a mantle source that is more depleted than the global average at slow-spreading ridges, which is inconsistent with the observed crustal thicknesses observed along the Mohns Ridge.

If the anomalous depleted mantle source was affected during the re-melting of a mantle depleted in enriched components because of a recent ridge jump (Sanfilippo et al., 2021), we might expect to see differences in the isotopic composition between the ridge basalts and basalts formed 4–5 Myr. However, the Sr and Nd isotopic ratios of the basalts (Table S1) are similar to those of the present-day spreading axis (Figures 4 and 5), implying that they have either (a) been derived from a similar source, or (b) been mixed and homogenized to such a degree that source compositions have been masked. Additional Hf-isotopic work may be required to further explore these hypotheses. Alternatively, the observed mantle depletion primarily records ancient melting events not related to the proposed ridge jump. At the Gakkel Ridge, Liu et al. (2008) used Re-Os systematics in peridotites to suggest ancient melt extraction took place as far back as 2 Ga. Earlier melting events at the Gakkel Ridge were further supported by geochemical and petrological investigations of dredged peridotites by D'Errico et al. (2016). Ancient melt depletion of the Mohns and Knipovich Ridge mantle has also been suggested based on Hf-isotope systematics of basalts (Sanfilippo et al., 2021). To explain the degree of partial melting estimated from the Schulz peridotites we consider that differences in the water content of the mantle source will have implications for the compositional evolution during partial melting, with the addition of water leading to faster depletion of pyroxene components (Gao et al., 2016; Kushiro, 1969). The steep MREE-HREE slopes and flat LREE-patterns of orthopyroxene (Figure 8) and recalculated whole-rock (Figure 9) resemble that of peridotites

from modern supra-subduction zones (Parkinson & Pearce, 1998). Interestingly, D'Errico et al. (2016) found similar REE-patterns for orthopyroxene at the Gakkel Ridge (Figure 8), suggesting that this is a widespread feature of the AMOR. An alternative explanation of the elevated LREE in the orthopyroxene (Figure 8) and recalculated whole-rock composition (Figure 9) is by adding a small percentage of trapped melt (e.g., Seyler et al., 2007). However, in the case of trapped melt, we would also expect an enrichment in elements like Ti, Y, and Zr (which is observed in orthopyroxene from GS16A-ROV6-004 and GS16A-ROV6-005 (Table S3)). The fact that we do not observe these enrichments, and rather, the orthopyroxene show low concentrations of these elements, makes us suggest that melt-rock interaction was not responsible for the elevated LREE. The observations above are therefore consistent with evidence from ocean ridge basalt compositions that indicates the mantle underlying much of the Arctic Ridges has a distinct subduction signature with high concentrations of H_2O (Yang et al., 2021). Both the peridotite and basalt chemistry presented here (Figures 3–5) is indicative of a subduction influence and suggests that the cause for the very-depleted mantle beneath much of the Arctic Ridges is because of an earlier hydrous melting event, likely in an arc setting. This is also supported by plate reconstructions (Alvey et al., 2008; Gaina et al., 2014; Shephard et al., 2013, 2016), seismic data (Lebedev et al., 2018), and geochemical considerations of erupted basalts (Richter et al., 2020; Yang et al., 2021), suggesting that a hydrous melting event in an arc environment is responsible for the observed depletion of the Arctic Mantle.

5.3. Mantle Source Isotopic Heterogeneity

The geochemical features of the peridotites and basalts suggest that a highly depleted, subduction-modified mantle is underlying the Mohns and Knipovich Ridges. The Nd-isotopic composition of orthopyroxene from samples GS16A-ROV6-003 and GS16A-ROV6-loc2 is much more enriched (i.e., lower $^{143}Nd/^{144}Nd$) than the expected mantle composition as sampled by the ridge lavas (Tables S1 and S4). There are two possible causes for the difference in isotopic composition. Either the signature is due to infiltration of seawater and alteration of the pyroxene, or it is inherited from the subduction influence. First, despite our attempt to pick the most pristine grains, these samples are heavily altered as described above and few grains appear completely fresh (Figures S1, S3, and S4 in Supporting Information S1). The extremely low Nd-concentration in low-Ti orthopyroxene from sample GS16A-ROV6-loc2, therefore, means that Nd potentially introduced during the alteration with seawater (e.g., Frisby et al., 2016) may account for a disproportionate part of the isotope signature. However, orthopyroxene from all samples shows similar alteration characteristics but does not appear to have been affected equally by seawater alteration. The alternative is that the isotopic composition reflects the subduction influence which would yield a very similar isotopic signature. Nd is mobile in slab-derived fluids (Kessel et al., 2005) and will potentially be imprinted in pyroxene during interaction with subduction-derived agents. Cipriani et al. (2004) found a relationship between the degree of partial melting and enrichment in $^{143}Nd/^{144}Nd$, suggesting that lowering of Nd isotopes was also associated with chemical enrichment (e.g., during infiltration of subduction-fluids). On the other hand, the Nd-isotope data on orthopyroxene from GS16A-ROV6-004 and GS16A-ROV6-005 overlap with the basalt compositions from Mohns Ridge and enriched basalts from the Lena Trough and Jan Mayen. We interpret this to reflect an isotopic re-equilibration associated with the localized infiltration of basaltic melts beneath the ridge axis. Taken together, the results from this study suggest the presence of an ancient, subduction-influenced mantle contained in the asthenosphere below the Mohns and Knipovich Ridges. The significance of this observation is that these highly depleted but isotopically enriched mantle rocks may reside in the suboceanic mantle and cannot represent the main source of the spreading-related magmatism which displays more depleted (i.e., higher $^{143}Nd/^{144}Nd$) isotopic signatures. However, the isotope data should be interpreted with caution and further work on additional isotope systems (e.g., Hf-isotopes (Bizimis et al., 2011)) may be required to validate this hypothesis.

6. Conclusions

In this study, abyssal peridotite geochemistry and mineral compositions were measured to constrain the process of mantle melting and to assess the mantle source beneath the paleo-Mohns ridge. Peridotites are harzburgites with estimated high degrees of partial melting from both Cr# of spinel and trace element modeling. The degrees of partial melting estimated from the peridotites are inconsistent with the observed and estimated crustal thickness in the area. Three independent sets of evidence suggest that the mantle has experienced hydrous melting in a subduction-type setting which has caused the anomalous degree of partial melting suggested by the peridotites.

First, the peridotites have low Al_2O_3 similar to arc-derived mantle rocks that experienced fluid-fluxed melting. Second, the trace element chemistry of basalts indicates a mantle source influenced by a water-rich slab flux. Finally, trace elements of orthopyroxene mimic that seen in peridotites from modern supra-subduction zone settings. Our results, therefore, provide evidence that the highly-depleted nature of the Mohns–Knipovich mantle is most likely because of an earlier recent hydrous mantle melting, likely an arc setting.

Data Availability Statement

All data generated during this study have been uploaded to the Zenodo data repository (Bjerga, Stubseid, Pedersen, Beinlich, & Pedersen, 2022), available under https://doi.org/10.5281/zenodo.7150300.

Acknowledgments
This work was funded by the K.G. Jebsen Foundation with support from the Norwegian Petroleum Directorate. Thanks to Yuval Ronen, Siv Dundas, Ole Tumyr, Irene Heggstad, and Muriel Erambert for assistance with geochemical analyses and laboratory work. Thanks to Peter Michael and an anonymous reviewer who significantly helped improve the manuscript.

References

Aldanmaz, E. (2012). Trace element geochemistry of primary mantle minerals in spinel-peridotites from polygenetic MOR–SSZ suites of SW Turkey: Constraints from an LA-ICP-MS study and implications for mantle metasomatism. *Geological Journal*, *47*(1), 59–76. https://doi.org/10.1002/gj.1336

Alvey, A., Gaina, C., Kusznir, N. J., & Torsvik, T. H. (2008). Integrated crustal thickness mapping and plate reconstructions for the high Arctic. *Earth and Planetary Science Letters*, *274*(3), 310–321. https://doi.org/10.1016/j.epsl.2008.07.036

Andres, M., Blichert-Toft, J., & Schilling, J.-G. (2004). Nature of the depleted upper mantle beneath the Atlantic: Evidence from Hf isotopes in normal mid-ocean ridge basalts from 79°N to 55°S. *Earth and Planetary Science Letters*, *225*(1), 89–103. https://doi.org/10.1016/j.epsl.2004.05.041

Barnes, S. J., & Roeder, P. L. (2001). The range of spinel compositions in terrestrial mafic and ultramafic rocks. *Journal of Petrology*, *42*(12), 2279–2302. https://doi.org/10.1093/petrology/42.12.2279

Bezard, R., Fischer-Gödde, M., Hamelin, C., Brennecka, G. A., & Kleine, T. (2016). The effects of magmatic processes and crustal recycling on the molybdenum stable isotopic composition of mid-ocean ridge basalts. *Earth and Planetary Science Letters*, *453*, 171–181. https://doi.org/10.1016/j.epsl.2016.07.056

Birner, S. K., Warren, J. M., Cottrell, E., Davis, F. A., Kelley, K. A., & Falloon, T. J. (2017). Forearc peridotites from Tonga record heterogeneous oxidation of the mantle following subduction initiation. *Journal of Petrology*, *58*(9), 1755–1780. https://doi.org/10.1093/petrology/egx072

Bizimis, M., Mallick, S., & Wallace, S. (2011). *First hafnium isotope data on mantle orthopyroxenes from Hawaiian peridotites* (pp. V31D–V2567). AGU Fall Meeting Abstracts.

Bjerga, A., Stubseid, H. H., Pedersen, L.-E. R., Beinlich, A., & Pedersen, R. B. (2022). A highly depleted and subduction-modified mantle beneath the slow-spreading Mohns Ridge. *Geochemistry, Geophysics, Geosystems*, *23*, e2022GC010585. https://doi.org/10.1029/2022gc010585 [Dataset].

Bjerga, A., Stubseid, H. H., Pedersen, L.-E. R., & Pedersen, R. B. (2022). Radiation damage allows identification of truly inherited zircon. *Communications Earth & Environment*, *3*(1), 37. https://doi.org/10.1038/s43247-022-00372-2

Blackman, D. K., & Collins, J. A. (2010). Lower crustal variability and the crust/mantle transition at the Atlantis Massif oceanic core complex. *Geophysical Research Letters*, *37*(24), L24303. https://doi.org/10.1029/2010gl045165

Blackman, D. K., Karson, J. A., Kelley, D. S., Cann, J. R., Fruh-Green, G. L., Gee, J. S., et al. (2002). Geology of the Atlantis massif (mid-Atlantic Ridge, 30°N): Implications for the evolution of an ultramafic oceanic core complex. *Marine Geophysical Researches*, *23*(5), 443–469. https://doi.org/10.1023/b:mari.0000018232.14085.75

Blichert-Toft, J., Agranier, A., Andres, M., Kingsley, R., Schilling, J. G., & Albarede, F. (2005). Geochemical segmentation of the Mid-Atlantic Ridge north of Iceland and ridge–hot spot interaction in the North Atlantic. *Geochemistry, Geophysics, Geosystems*, *6*(1), Q01E19. https://doi.org/10.1029/2004gc000788

Brandon, A. D., Snow, J. E., Walker, R. J., Morgan, J. W., & Mock, T. D. (2000). 190Pt–186Os and 187Re–187Os systematics of abyssal peridotites. *Earth and Planetary Science Letters*, *177*(3), 319–335. https://doi.org/10.1016/s0012-821x(00)00044-3

Brunelli, D., Cipriani, A., & Bonatti, E. (2018). Thermal effects of pyroxenites on mantle melting below mid-ocean ridges. *Nature Geoscience*, *11*(7), 520–525. https://doi.org/10.1038/s41561-018-0139-z

Bruvoll, V., Breivik, A. J., Mjelde, R., & Pedersen, R. B. (2009). Burial of the Mohn-Knipovich seafloor spreading ridge by the Bear Island Fan: Time constraints on tectonic evolution from seismic stratigraphy. *Tectonics*, *28*(4). https://doi.org/10.1029/2008tc002396

Burgath, K.-P., Marchig, V., & Mussallam, K. (1997). 29. Data report: Mineralogic, structural, and chemical variability of mantle sections from Holes 920B and 920D. In *Proceedings ODP* (p. 153). Science Results College Station.

Byerly, B. L., & Lassiter, J. C. (2014). Isotopically ultradepleted domains in the convecting upper mantle: Implications for MORB petrogenesis. *Geology*, *42*(3), 203–206. https://doi.org/10.1130/g34757.1

Ciazela, J., Koepke, J., Dick, H. J., & Muszynski, A. J. G. (2015). Mantle rock exposures at oceanic core complexes along mid-ocean ridges. *Geologos*, *21*(4), 207–231. https://doi.org/10.1515/logos-2015-0017

Cipriani, A., Brueckner, H. K., Bonatti, E., & Brunelli, D. (2004). Oceanic crust generated by elusive parents: Sr and Nd isotopes in basalt-peridotite pairs from the Mid-Atlantic Ridge. *Geology*, *32*(8), 657–660. https://doi.org/10.1130/g20560.1

Coogan, L. A., Thompson, G., MacLeod, C., Dick, H., Edwards, S., Hosford Scheirer, A., & Barry, T. (2004). A combined basalt and peridotite perspective on 14 million years of melt generation at the Atlantis Bank segment of the Southwest Indian Ridge: Evidence for temporal changes in mantle dynamics? *Chemical Geology*, *207*(1), 13–30. https://doi.org/10.1016/j.chemgeo.2004.01.016

D'Errico, M. E., Warren, J. M., & Godard, M. (2016). Evidence for chemically heterogeneous Arctic mantle beneath the Gakkel Ridge. *Geochimica et Cosmochimica Acta*, *174*, 291–312. https://doi.org/10.1016/j.gca.2015.11.017

Deschamps, F., Godard, M., Guillot, S., & Hattori, K. (2013). Geochemistry of subduction zone serpentinites: A review. *Lithos*, *178*, 96–127. https://doi.org/10.1016/j.lithos.2013.05.019

Detrick, R. S., Needham, H. D., & Renard, V. (1995). Gravity anomalies and crustal thickness variations along the Mid-Atlantic Ridge between 33°N and 40°N. *Journal of Geophysical Research*, *100*(B3), 3767–3787. https://doi.org/10.1029/94jb02649

Dick, H. J. B., Fisher, R. L., & Bryan, W. B. (1984). Mineralogic variability of the uppermost mantle along mid-ocean ridges. *Earth and Planetary Science Letters*, *69*(1), 88–106. https://doi.org/10.1016/0012-821x(84)90076-1

Dick, H. J. B., Lissenberg, C. J., & Warren, J. M. (2010). Mantle melting, melt transport, and delivery beneath a slow-spreading ridge: The Paleo-MAR from 23°15′N to 23°45′N. *Journal of Petrology*, *51*(1–2), 425–467. https://doi.org/10.1093/petrology/egp088

Dick, H. J. B., Tivey, M. A., & Tucholke, B. E. (2008). Plutonic foundation of a slow-spreading ridge segment: Oceanic core complex at Kane Megamullion, 23°30′N, 45°20′W. *Geochemistry, Geophysics, Geosystems*, *9*(5), Q05014. https://doi.org/10.1029/2007gc001645

Dosso, L., Bougault, H., Langmuir, C., Bollinger, C., Bonnier, O., & Etoubleau, J. (1999). The age and distribution of mantle heterogeneity along the Mid-Atlantic Ridge (31–41°N). *Earth and Planetary Science Letters*, *170*(3), 269–286. https://doi.org/10.1016/s0012-821x(99)00109-0

Drouin, M., Godard, M., Ildefonse, B., Bruguier, O., & Garrido, C. J. (2009). Geochemical and petrographic evidence for magmatic impregnation in the oceanic lithosphere at Atlantis Massif, Mid-Atlantic Ridge (IODP Hole U1309D, 30°N). *Chemical Geology*, *264*(1), 71–88. https://doi.org/10.1016/j.chemgeo.2009.02.013

Frisby, C., Bizimis, M., & Mallick, S. (2016). Seawater-derived rare Earth element addition to abyssal peridotites during serpentinization. *Lithos*, *248–251*, 432–454. https://doi.org/10.1016/j.lithos.2016.01.025

Gaina, C., Medvedev, S., Torsvik, T. H., Koulakov, I., & Werner, S. C. (2014). 4D Arctic: A glimpse into the structure and evolution of the Arctic in the light of new geophysical maps, plate tectonics and tomographic models. *Surveys in Geophysics*, *35*(5), 1095–1122. https://doi.org/10.1007/s10712-013-9254-y

Gale, A., Dalton, C. A., Langmuir, C. H., Su, Y., & Schilling, J.-G. (2013). The mean composition of ocean ridge basalts. *Geochemistry, Geophysics, Geosystems*, *14*(3), 489–518. https://doi.org/10.1029/2012gc004334

Gao, C., Dick, H. J. B., Liu, Y., & Zhou, H. (2016). Melt extraction and mantle source at a Southwest Indian ridge Dragon Bone amagmatic segment on the marion rise. *Lithos*, *246–247*, 48–60. https://doi.org/10.1016/j.lithos.2015.12.007

Garrido, C. J., Bodinier, J.-L., & Alard, O. (2000). Incompatible trace element partitioning and residence in anhydrous spinel peridotites and websterites from the Ronda orogenic peridotite. *Earth and Planetary Science Letters*, *181*(3), 341–358. https://doi.org/10.1016/s0012-821x(00)00201-6

Godard, M., Awaji, S., Hansen, H., Hellebrand, E., Brunelli, D., Johnson, K., et al. (2009). Geochemistry of a long in-situ section of intrusive slow-spread oceanic lithosphere: Results from IODP Site U1309 (Atlantis Massif, 30°N Mid-Atlantic-Ridge). *Earth and Planetary Science Letters*, *279*(1), 110–122. https://doi.org/10.1016/j.epsl.2008.12.034

Godard, M., Lagabrielle, Y., Alard, O., & Harvey, J. (2008). Geochemistry of the highly depleted peridotites drilled at ODP Sites 1272 and 1274 (Fifteen-Twenty Fracture Zone, Mid-Atlantic Ridge): Implications for mantle dynamics beneath a slow spreading ridge. *Earth and Planetary Science Letters*, *267*(3), 410–425. https://doi.org/10.1016/j.epsl.2007.11.058

Goldstein, S. L., Soffer, G., Langmuir, C. H., Lehnert, K. A., Graham, D. W., & Michael, P. J. (2008). Origin of a "Southern Hemisphere" geochemical signature in the Arctic upper mantle. *Nature*, *453*(7191), 89–93. https://doi.org/10.1038/nature06919

Graham, D. W., Blichert-Toft, J., Russo, C. J., Rubin, K. H., & Albarède, F. (2006). Cryptic striations in the upper mantle revealed by hafnium isotopes in southeast Indian ridge basalts. *Nature*, *440*(7081), 199–202. https://doi.org/10.1038/nature04582

Guo, P., Niu, Y., Sun, P., Zhang, J., Chen, S., Duan, M., et al. (2021). The nature and origin of upper mantle heterogeneity beneath the mid-Atlantic Ridge 33–35°N: A Sr-Nd-Hf isotopic perspective. *Geochimica et Cosmochimica Acta*, *307*, 72–85. https://doi.org/10.1016/j.gca.2021.05.033

Haase, K. M., Devey, C. W., Mertz, D. F., Stoffers, P., & Garbe-Schönberg, D. (1996). Geochemistry of lavas from Mohns Ridge, Norwegian-Greenland Sea: Implications for melting conditions and magma sources near Jan mayen. *Contributions to Mineralogy and Petrology*, *123*(3), 223–237. https://doi.org/10.1007/s004100050152

Harvey, J., Gannoun, A., Burton, K. W., Rogers, N. W., Alard, O., & Parkinson, I. J. (2006). Ancient melt extraction from the oceanic upper mantle revealed by Re–Os isotopes in abyssal peridotites from the Mid-Atlantic ridge. *Earth and Planetary Science Letters*, *244*(3), 606–621. https://doi.org/10.1016/j.epsl.2006.02.031

Hauri, E. H. (2002). Osmium isotopes and mantle convection. *Philosophical Transactions of the Royal Society A*, *360*(1800), 2371–2382. https://doi.org/10.1098/rsta.2002.1073

Hellebrand, E., Snow, J. E., Dick, H. J. B., & Hofmann, A. W. (2001). Coupled major and trace elements as indicators of the extent of melting in mid-ocean-ridge peridotites. *Nature*, *410*(6829), 677–681. https://doi.org/10.1038/35070546

Hellebrand, E., Snow, J. E., Hoppe, P., & Hofmann, A. W. (2002). Garnet-field melting and late-stage refertilization in "residual"abyssal peridotites from the Central Indian Ridge. *Journal of Petrology*, *43*(12), 2305–2338. https://doi.org/10.1093/petrology/43.12.2305

John, B. E., Foster, D. A., Murphy, J. M., Cheadle, M. J., Baines, A., Fanning, C., & Copeland, P. (2004). Determining the cooling history of in situ lower oceanic crust—Atlantis Bank, SW Indian ridge. *Earth and Planetary Science Letters*, *222*(1), 145–160. https://doi.org/10.1016/j.epsl.2004.02.014

Johnson, K. T. M., Dick, H. J. B., & Shimizu, N. (1990). Melting in the oceanic upper mantle: An ion microprobe study of diopsides in abyssal peridotites. *Journal of Geophysical Research*, *95*(B3), 2661–2678. https://doi.org/10.1029/jb095ib03p02661

Kelley, K. A., Kingsley, R., & Schilling, J.-G. (2013). Composition of plume-influenced mid-ocean ridge lavas and glasses from the mid-Atlantic Ridge, east Pacific rise, Galápagos spreading Center, and Gulf of Aden. *Geochemistry, Geophysics, Geosystems*, *14*(1), 223–242. https://doi.org/10.1002/ggge.20049

Kenyon, S., Forsberg, R., & Coakley, B. (2008). New gravity field for the Arctic. *Eos, Transactions American Geophysical Union*, *89*(32), 289–290. https://doi.org/10.1029/2008eo320002

Kessel, R., Schmidt, M. W., Ulmer, P., & Pettke, T. (2005). Trace element signature of subduction-zone fluids, melts and supercritical liquids at 120–180 km depth. *Nature*, *437*(7059), 724–727. https://doi.org/10.1038/nature03971

Klein, E. M., & Langmuir, C. H. (1987). Global correlations of ocean ridge basalt chemistry with axial depth and crustal thickness. *Journal of Geophysical Research*, *92*(B4), 8089–8115. https://doi.org/10.1029/jb092ib08p08089

Klingelhöfer, F., Géli, L., Matias, L., Steinsland, N., & Mohr, J. (2000). Crustal structure of a super-slow spreading centre:a seismic refraction study of Mohns Ridge, 72°N. *Geophysical Journal International*, *141*(2), 509–526. https://doi.org/10.1046/j.1365-246x.2000.00098.x

Kruber, C., Thorseth, I. H., & Pedersen, R. B. (2008). Seafloor alteration of basaltic glass: Textures, geochemistry, and endolithic microorganisms. *Geochemistry, Geophysics, Geosystems*, *9*(12), Q12002. https://doi.org/10.1029/2008gc002119

Kushiro, I. (1969). The system forsterite-diopside-silica with and without water at high pressures. *American Journal of Science*, *267*(A), 269–294.

Lassiter, J. C., Byerly, B. L., Snow, J. E., & Hellebrand, E. (2014). Constraints from Os-isotope variations on the origin of Lena Trough abyssal peridotites and implications for the composition and evolution of the depleted upper mantle. *Earth and Planetary Science Letters*, *403*, 178–187. https://doi.org/10.1016/j.epsl.2014.05.033

Lebedev, S., Schaeffer, A. J., Fullea, J., & Pease, V. (2018). Seismic tomography of the Arctic region: Inferences for the thermal structure and evolution of the lithosphere. In *Circum-arctic lithosphere evolution*. The Geological Society of London.

Liu, C.-Z., Snow, J. E., Hellebrand, E., Brugmann, G., von der Handt, A., Buchl, A., & Hofmann, A. W. (2008). Ancient, highly heterogeneous mantle beneath Gakkel ridge, Arctic Ocean. *Nature*, *452*(7185), 311–316. https://doi.org/10.1038/nature06688

Liu, P.-P., Teng, F.-Z., Dick, H. J. B., Zhou, M.-F., & Chung, S.-L. (2017). Magnesium isotopic composition of the oceanic mantle and oceanic Mg cycling. *Geochimica et Cosmochimica Acta*, *206*, 151–165. https://doi.org/10.1016/j.gca.2017.02.016

Mallick, S., Dick, H. J. B., Sachi-Kocher, A., & Salters, V. J. M. (2014). Isotope and trace element insights into heterogeneity of subridge mantle. *Geochemistry, Geophysics, Geosystems*, *15*(6), 2438–2453. https://doi.org/10.1002/2014gc005314

Maus, S., Barckhausen, U., Berkenbosch, H., Bournas, N., Brozena, J., Childers, V., et al. (2009). EMAG2: A 2–arc min resolution Earth magnetic anomaly grid compiled from satellite, airborne, and marine magnetic measurements. *Geochemistry, Geophysics, Geosystems*, *10*(8), Q08005. https://doi.org/10.1029/2009gc002471

McDonough, W. F., & Sun, S. S. (1995). The composition of the Earth. *Chemical Geology*, *120*(3–4), 223–253. https://doi.org/10.1016/0009-2541(94)00140-4

Merlini, A., Grieco, G., & Diella, V. (2009). Ferritchromite and chromian-chlorite formation in melange-hosted Kalkan chromitite (Southern Urals, Russia). *American Mineralogist*, *94*(10), 1459–1467. https://doi.org/10.2138/am.2009.3082

Müller, R. D., Sdrolias, M., Gaina, C., & Roest, W. R. (2008). Age, spreading rates, and spreading asymmetry of the world's ocean crust. *Geochemistry, Geophysics, Geosystems*, *9*(4), Q04006. https://doi.org/10.1029/2007gc001743

Neumann, E.-R., & Schilling, J.-G. (1984). Petrology of basalts from the Mohns-Knipovich ridge; the Norwegian-Greenland Sea. *Contributions to Mineralogy and Petrology*, *85*(3), 209–223. https://doi.org/10.1007/bf00378101

Niu, Y. (2004). Bulk-rock major and trace element compositions of abyssal peridotites: Implications for mantle melting, melt extraction and post-melting processes beneath mid-ocean ridges. *Journal of Petrology*, *45*(12), 2423–2458. https://doi.org/10.1093/petrology/egh068

Parkinson, I. J., & Pearce, J. A. (1998). Peridotites from the Izu–Bonin–Mariana Forearc (ODP Leg 125): Evidence for mantle melting and melt–mantle interaction in a supra-subduction zone setting. *Journal of Petrology*, *39*(9), 1577–1618. https://doi.org/10.1093/petroj/39.9.1577

Pearce, J. A., Barker, P. F., Edwards, S. J., Parkinson, I. J., & Leat, P. T. (2000). Geochemistry and tectonic significance of peridotites from the South Sandwich arc–basin system, South Atlantic. *Contributions to Mineralogy and Petrology*, *139*(1), 36–53. https://doi.org/10.1007/s004100050572

Rampone, E., & Hofmann, A. W. (2012). A global overview of isotopic heterogeneities in the oceanic mantle. *Lithos*, *148*, 247–261. https://doi.org/10.1016/j.lithos.2012.06.018

Regelous, M., Weinzierl, C. G., & Haase, K. M. (2016). Controls on melting at spreading ridges from correlated abyssal peridotite—Mid-Ocean ridge basalt compositions. *Earth and Planetary Science Letters*, *449*, 1–11. https://doi.org/10.1016/j.epsl.2016.05.017

Richter, M., Nebel, O., Maas, R., Mather, B., Nebel-Jacobsen, Y., Capitanio, F. A., et al. (2020). An early cretaceous subduction-modified mantle underneath the ultraslow spreading Gakkel Ridge, Arctic Ocean. *Science Advances*, *6*(44). https://doi.org/10.1126/sciadv.abb4340

Sanfilippo, A., Salters, V. J. M., Sokolov, S. Y., Peyve, A. A., & Stracke, A. (2021). Ancient refractory asthenosphere revealed by mantle re-melting at the Arctic Mid Atlantic Ridge. *Earth and Planetary Science Letters*, *566*, 116981. https://doi.org/10.1016/j.epsl.2021.116981

Scott, J. M., Liu, J., Pearson, D. G., & Waight, T. E. (2016). Mantle depletion and metasomatism recorded in orthopyroxene in highly depleted peridotites. *Chemical Geology*, *441*, 280–291. https://doi.org/10.1016/j.chemgeo.2016.08.024

Seyler, M., Lorand, J. P., Dick, H. J. B., & Drouin, M. (2007). Pervasive melt percolation reactions in ultra-depleted refractory harzburgites at the Mid-Atlantic Ridge, 15° 20′N: ODP Hole 1274A. *Contributions to Mineralogy and Petrology*, *153*(3), 303–319. https://doi.org/10.1007/s00410-006-0148-6

Shephard, G. E., Müller, R. D., & Seton, M. (2013). The tectonic evolution of the Arctic since Pangea breakup: Integrating constraints from surface geology and geophysics with mantle structure. *Earth-Science Reviews*, *124*, 148–183. https://doi.org/10.1016/j.earscirev.2013.05.012

Shephard, G. E., Trønnes, R. G., Spakman, W., Panet, I., & Gaina, C. (2016). Evidence for slab material under Greenland and links to cretaceous high Arctic magmatism. *Geophysical Research Letters*, *43*(8), 3717–3726. https://doi.org/10.1002/2016gl068424

Stracke, A. (2012). Earth's heterogeneous mantle: A product of convection-driven interaction between crust and mantle. *Chemical Geology*, *330–331*, 274–299. https://doi.org/10.1016/j.chemgeo.2012.08.007

Stracke, A., & Bourdon, B. (2009). The importance of melt extraction for tracing mantle heterogeneity. *Geochimica et Cosmochimica Acta*, *73*(1), 218–238. https://doi.org/10.1016/j.gca.2008.10.015

Stracke, A., Genske, F., Berndt, J., & Koornneef, J. M. (2019). Ubiquitous ultra-depleted domains in Earth's mantle. *Nature Geoscience*, *12*(10), 851–855. https://doi.org/10.1038/s41561-019-0446-z

Urann, B. M., Dick, H. J. B., Parnell-Turner, R., & Casey, J. F. (2020). Recycled arc mantle recovered from the Mid-Atlantic Ridge. *Nature Communications*, *11*(1), 3887. https://doi.org/10.1038/s41467-020-17604-8

Warren, J. M. (2016). Global variations in abyssal peridotite compositions. *Lithos*, *248–251*, 193–219. https://doi.org/10.1016/j.lithos.2015.12.023

Warren, J. M., Shimizu, N., Sakaguchi, C., Dick, H. J. B., & Nakamura, E. (2009). An assessment of upper mantle heterogeneity based on abyssal peridotite isotopic compositions. *Journal of Geophysical Research*, *114*(B12), B12203. https://doi.org/10.1029/2008jb006186

Workman, R. K., & Hart, S. R. (2005). Major and trace element composition of the depleted MORB mantle (DMM). *Earth and Planetary Science Letters*, *231*(1), 53–72. https://doi.org/10.1016/j.epsl.2004.12.005

Yang, A. Y., Langmuir, C. H., Cai, Y., Michael, P., Goldstein, S. L., & Chen, Z. (2021). A subduction influence on ocean ridge basalts outside the Pacific subduction shield. *Nature Communications*, *12*(1), 4757. https://doi.org/10.1038/s41467-021-25027-2

References From the Supporting Information

Deniel, C., & Pin, C. (2001). Single-stage method for the simultaneous isolation of lead and strontium from silicate samples for isotopic measurements. *Analytica Chimica Acta*, *426*(1), 95–103. https://doi.org/10.1016/s0003-2670(00)01185-5

Govindaraju, K. (1994). 1994 compilation of working values and sample description for 383 geostandards. *Geostandards and Geoanalytical Research*, *18*, 1–158. https://doi.org/10.1046/j.1365-2494.1998.53202081.x-i1

Howell, D., Griffin, W., Pearson, N., Powell, W., Wieland, P., & O'Reilly, S. (2013). Trace element partitioning in mixed-habit diamonds. *Chemical Geology*, *355*, 134–143. https://doi.org/10.1016/j.chemgeo.2013.07.013

Longerich, H. P., Jackson, S. E., & Günther, D. (1996). Inter-laboratory note. Laser ablation inductively coupled plasma mass spectrometric transient signal data acquisition and analyte concentration calculation. *Journal of Analytical Atomic Spectrometry*, *11*(9), 899–904. https://doi.org/10.1039/ja9961100899

Paton, C., Hellstrom, J., Paul, B., Woodhead, J., & Hergt, J. (2011). Iolite: Freeware for the visualisation and processing of mass spectrometric data. *Journal of Analytical Atomic Spectrometry*, *26*(12), 2508. https://doi.org/10.1039/c1ja10172b

Paton, C., Woodhead, J. D., Hellstrom, J. C., Hergt, J. M., Greig, A., & Maas, R. (2010). Improved laser ablation U-Pb zircon geochronology through robust downhole fractionation correction. *Geochemistry, Geophysics, Geosystems*, *11*(3), Q0AA06. https://doi.org/10.1029/2009gc002618

Plumlee, G. (1998). United States geological survey certificate of analysis: Basalt.

Richard, P., Shimizu, N., & Allègre, C. J. (1976). 143Nd/146Nd, a natural tracer: An application to oceanic basalts. *Earth and Planetary Science Letters*, *31*(2), 269–278. https://doi.org/10.1016/0012-821x(76)90219-3